The
University
Of
Sheffield.

This is a repository copy of *Guar gum: A novel binder for ceramic extrusion*.

White Rose
university consortium
Universities of Leeds, Sheffield & York

eprints@whiterose.ac.uk
https://eprints.whiterose.ac.uk/

# Guar Gum: A Novel Binder for Ceramic Extrusion

M. Elbadawi [1*], M.Mosalagae [2], I.M.Reaney [2], J.Meredith [1].

[1] Department of Mechanical Engineering, University of Sheffield, Mappin Street, Sheffield, S1 3JD, United Kingdom.

[2] Department of Material Science and Engineering, University of Sheffield, Mappin Street, Sheffield, S1 3JD, United Kingdom.

[*]Corresponding author, email: melbadawi1@sheffield.ac.uk

## 1    Abstract

Ceramic honeycomb extrusion is a technique capable of attaining high strength, porous ceramics. However, challenges prevent the realisation of its potential. These include the design of an intricate honeycomb die and the formulation of an extrudable paste. The present study addresses the latter by using guar gum (GG) as a binder. GG was rationally selected because hydrogels thereof exhibit strong shear-thinning and high stiffness properties, which are required for extrusion. Rheological analyses demonstrated ceramic pastes with similar qualities were achieved, with hydroxyapatite (HA) used as the model ceramic. The shear stiffness modulus of HA pastes was determined as 8.4 MPa with a yield stress of 1.1 kPa. Moreover, this was achieved with GG as the sole additive, which further facilitates the overall fabrication process. The binder extraction notably occurred at relatively low temperatures when other high molecular weight polymers demand temperatures above 1000 °C; therefore the latter precludes the use of ceramics with low sintering onset. The process culminated in a porous HA scaffold with similar porosity to that of a commercial HA graft, but with higher compressive strength. Lastly, the study

notes that the biological and water-soluble properties of GG can broaden its application into other ceramic fabrication processes.

**Keywords:** Extrusion (A); Strength (C); Biomedical application (E); Guar Gum.

## 2    Introduction

Porous ceramics continue to be a subject of interest for many functional ceramic applications. In the field of bioceramics, a porous bone graft is required due to the benefits elicited by the pores, which include new bone formation, vascularisation and oxygen nutrient transport [1-4]. However, given that porosity and mechanical strength are mutually exclusive, it has proven difficult to form porous bioceramic scaffolds with sufficient strength using traditional fabrication methods [5, 6].

Ceramic honeycomb extrusion is one technique capable of achieving high mechanical properties, [7, 8] which is partly attributed to its periodic porous architecture [9, 10]. Hence, there is potential for the technique in the fabrication of synthetic bone grafts.  Like other fabrication techniques, including solid free-form fabrication, which are considered as state of the art, ceramic extrusion necessitates the use of binders. Methylcellulose (MC), and other cellulose-derived polymers are heavily relied on as the primary binder [11-16]. One concern with using MC is its thermal gelation property [17], whereby the polymer crosslinks at high temperatures and hardens. Thermal gelation of MC occurs typically at ~ 50 °C, and as the processing temperature nears the thermal gelation point, the viscosity increases exponentially. Thus, fabrication techniques using MC require additional control to preclude processing above 50 °C that can lead to defects, such as crack formation [18].

2

Guar gum is another water-soluble polysaccharide capable of forming a gel network ideal for the suspension of ceramic particles. Guar gum (GG) is an industrial gum with a number of applications [19]. GG has a molecular weight ranging from 0.2 to 5.0 million, the highest of the water-soluble polysaccharides, and hence are able to impart high viscosity. This can be achieved at low concentrations [20], which is desirable in ceramic extrusion as high viscosity is needed to impart green strength whilst low binder concentrations ensures a high ceramic solids loading can be achieved. This will lower the probability of defects appearing post-extrusion, particularly during shrinkage. Moreover, in bioceramics, GG is attractive as it is nontoxic, biocompatible and biodegradable [21], and thus can be used in cell-laden processes. In contrast to MC, GG is not affected by thermal gelation [22], thus facilitating processing of ceramics when selected as the binder.

The aim of this article is to examine the suitability of GG as a binder for ceramic honeycomb extrusion, using hydroxyapatite as the model ceramic. The central part of the study seeks to explore its potential through rheological characterisation, as well as determining a suitable thermal debinding profile. The characteristics of the hydroxyapatite scaffolds, with respect to mechanical, porosity and microstructural properties are also reported.

## 3    Materials and Method

## 3.1    Raw Materials

Commercially available hydroxyapatite powder (Purum grade, Sigma Aldrich) pre-calcined at 1000 °C, and GG (Lot no.: SLBH5231V; Sigma Aldrich) were used for this study. **Fig. 1** depicts the powder morphology of the GG powder. Distilled water was used as the solvent.

## 3.2    Fabrication Procedure

Mixing was carried out in two stages. First, the dry components (ceramic and binder) were weighed and then mixed using a high-energy speed mixer (Speedmixer™ DAC 300FVZ, Synergy Devices Limited) to ensure a homogenous distribution of the ceramic component and polymer. Solvent was then added in two minute intervals, until a single coalesced paste was obtained. Mixing was continued for a further 5 minutes following coalescence of the ceramic paste. Once a suitable paste was obtained, it was extruded using an in-house ram extruder and honeycomb die (**Fig. 2**). The die comprised feed holes of 1.2 mm and distance of 1.52 mm apart; and die pins with a width of ~ 1 mm. The pastes were next loaded into the barrel of the extruder, and placed under vacuum (i.e. deaired) prior to extrusion. A servo-hydraulic press (Schenck 250 kN) was employed to actuate the piston. The extrudates were dried for twenty-four hours, at ambient temperatures. The extrudates were then thermally debound in a muffle furnace (Elite Thermal Systems Ltd). The thermal debinding process is detailed in the results section. The extrudates were subsequently sintered in a muffle furnace at 1250 °C using a heating rate of 5 °C/min. For further characterisations, the extrudates were sectioned into ~ 4.5 mm$^3$ cubes (Isomet® 250, Buehler), and ground flat using silicon carbide grinding paper. A total of ten scaffolds were fashioned from three extrudates.

## 3.3    Characterisation

### 3.3.1    Rheological

Viscosity measurements of the pastes were performed using Malvern's Rosand RH200 15 mm twin bore capillary rheometer, and the experimental procedure was selected using the Flowmaster™ software. A tungsten carbide die with a diameter, length and angle of

4

1 mm, 16 mm and 180 °, respectively, was used. Before each measurement, the samples were kneaded by hand and loaded into the barrel at ambient temperature, followed by manual compaction using a piston to a reference point (95-110 mm).

To compliment the capillary rheometry analysis, a rotational rheometer was employed in oscillatory mode, also referred to as dynamic mechanical analysis (DMA), to elucidate the mechanical behaviour of pastes. By performing an amplitude sweep test, whereby subjecting samples to increasing oscillatory forces, a shear stress-strain curve was obtained. From the data, the shear modulus and the plastic behaviour of samples were determined. The former is akin to the elastic modulus, however, as the instrument applies a torsional force, rather than an axial force, it is the shear characteristics that were analysed. The DMA data was used in correlation to the capillary rheometer data to determine the quality of the extrudates. The rotational rheometer (MCR 302, Anton Paar) was equipped with an 8-mm parallel plate geometry, and controlled using Rheoplus software. As ceramic pastes are classified as high-viscous materials, an 8-mm plate geometry was selected, capable of generating high rheological stresses. The speed of the test was empirically determined to ensure that measurements can be recorded before the paste ages. Care was taken not to omit key transition points. When working with relatively low solvent slurries, ageing can occur if the test is unnecessarily prolonged, consequently leading to erroneous measurements. Accordingly, the following parameters were selected: the initial and final strain were 0.001 and 20%, respectively; the frequency was set to 50 rad/s; and the plate gap was set to 0.5 mm.

The MOOG SmarTEST ONE controller, which was used to control the servo-hydraulic press was also used to record the force feedback as a function of piston travel,

and thus producing force-displacement curves. Sampling was performed at a recording frequency of 100 Hz.

### 3.3.2   Thermal

TGA analysis was performed to determine the change in sample mass as a function of temperature, using Perkin Elmer's Pyris TGA 1 and alumina pans, and controlled using the Pyris software.

### 3.3.3   Spectroscopy

Fourier-transformation-infrared (FTIR) spectroscopy was performed using the Perkin Elmer Frontier, and operated using the Spectrum software. First, the powder samples were mixed with potassium bromide (KBr) at a ratio of 2:200 mg using an agate pestle and mortar. Once sufficiently mixed and the admixture was homogenous, samples were pressed into a disc using a 10 mm stainless steel pellet die; the force was first applied at 1 ton for one minute, and then increased to 10 tons for a further one minute. Once pressed, the samples were inserted into the sample holder, and subsequently placed into the instrument for analysis.

### 3.3.4   Microscopy

Scanning electron microscopy (SEM) analysis was performed to examine the microstructure of the scaffolds. Samples were coated with gold prior to examination, using a SC 500A, Emscope sputter system. Optical microscopy was employed to measure the macro-pore sizes using the Motic®'s BA310Met-T microscope, fitted with Moticam 3 attachable digital C-mount camera, and controlled by the Motic Images Plus software.

### 3.3.5 Physical Properties

A gas helium pycnometer (Accupyc II 1340, Micromeritics) was utilised for measuring the true scaffold volume, which was subtracted from the apparent volume to give the bulk porosity (n=3). A vernier caliper was used to measure the apparent volume, which was taken as the three dimensions illustrated in **Fig. 3**. Although bone is subjected to different forms of stress, compressive strength is used as the benchmark indicator for mechanical properties. Tests were performed using the the Zwick Roell Z050, with a 20 kN load cell (Xforce K, Zwick; 0.5% resolution), and operated by the testXpert II software.

## 4    Results and discussion

### 4.1    Paste Rheology

A hydroxyapatite paste formulated using GG as the sole organic additive was successfully fabricated. The solids loading achieved was 62 wt%, and pastes were notably stiff. To ensure the newly formulated admixture possessed the correct flow characteristics for ceramic extrusion, rheological characterisation was conducted.

### 4.1.1    Capillary Rheometry

For a defect-free extrusion of honeycomb structures, it is essential that the paste satisfies both a non-newtonian flow behaviour and should have sufficient strength to main structural integrity thereafter [14]. A capillary rheometer was used to determine the flow characteristics of HA pastes formulated using guar gum as a binder, with the results illustrated in **Fig. 4**. Capillary rheometer analysis (**Fig. 4 (a)**) revealed that the admixture was capable of exhibiting shear-thinning behaviour, which is defined as a decrease in shear viscosity ($\eta$) with increasing shear rate ($\gamma$), and is a requirement for defect-free

ceramic extrusion. Shear-thinning is a property of ceramic slurries and pastes, wherein the polymer chains, which are initially oriented in different directions within the admixture, are disentangled when enough force is applied. The resistance to flow decreases as the disentanglement progresses, eventually resulting in a flowing admixture when the polymers are oriented to the direction of flow (**Fig. 5**).

In honeycomb extrusion, the pastes are first sheared as they enter the feeder holes of the die and are then required to reknit thereafter to form the desired geometry (**Fig. 6**). Thus, strong shear-thinning is favourable as less force is required for the convergence of adjacent sheared layers but the value should not be too low that the paste is easily sheared resulting in lamination defects.

### 4.1.2 Dynamic Mechanical Analysis (DMA) – Amplitude Sweep

The plastic behaviour of ceramic pastes is generally predicted by stress–deformation compression curves [23], hence dynamic mechanical analysis was utilised. **Fig. 7** is the DMA data for the GG paste. The curve illustrates that at low shear stress, the paste displays constant plateau values, which is termed the linear viscoelastic (LVE) range [24, 25]. Here, the material displays elastic behaviour and is able to return to its original shape when the load is withdrawn. The point of inflexion (denoted by the arrows) is termed the yield point, at which the elastic limit of the material is reached and begins to exhibit plastic deformation thereafter.

The analysis revealed that the GG possessed a shear stiffness modulus of 8.4 MPa, and a yield stress value of 1.1 kPa (**$Y_{s1}$**). Following the yield point, the paste remained plastic until the end of the test, which was nearly by a factor of two orders of a magnitude.

The pastes were immediately tested again were it was revealed that a marginal decrease in mechanical properties had occurred, thus demonstrating that the pastes were able to maintain their high stiffness after being subjected to shear stress. The storage modulus and yield stress decreased to 4.3 MPa and 0.85 kPa, respectively. The wide plasticity region of GG highlights the excellent workability it imparts onto ceramic pastes. This characteristic conflicts with that of other pastes in which high stress and plastic deformation are mutually exclusive [26].

### 4.1.3   Extrusion Plot

Paste extrusion pressure as a function of distance travelled by the piston was recorded in situ, as portrayed in **Fig. 8**. For comparison, a recorded plot of a common binder (Methocel™ (methylcellulose)) with comparable paste composition from a study to be reported by the authors, was included. The Methocel™ (MC) curve is typical of what has been previously recorded in force-displacement extrusion plots [20, 27, 28]. As the figure delineates, MC displayed an initial linear increase in force as the piston began to travel and the paste made contact with the die. Subsequently a drop in pressure was observed, which reflects the material exiting the die. Here, the paste maintained a plateau. GG pastes on the other hand presented with a moderate decrease following the pressure drop that continued until the end of the run. Despite possessing a markedly higher extrusion force prior to exiting the die than that of MC, there was an eventual overlap. The resultant GG extrudates were sufficiently strong immediately after extruding.

The data confirms GG's contrasting rheological properties. The high extrusion force required is attributed to GG possessing a higher viscosity in comparison to MC, whereas the lack of a plateau following the pressure drop can be ascribed to its strongly

9

shear-thinning properties [29]. It should be noted that the extrusion force recorded was higher than what has been previously reported. This was due to the considerably high extrusion rate used, which is known to affect the extrusion force [30]. The high extrusion rate used in the present study was found to yield a defect-free extrudate during preliminary investigations. However, as **Fig. 4** (**a**) conveys, GG pastes can flow at lower shear rates. **Fig. 9** is representative image depicting the result of the extruded paste through the honeycomb die. Typical defects associated with ceramic extrusion were not observed.

The rheological analyses corroborated that ceramic pastes formulated using GG have excellent stiffness and shear-thinning properties. The rheological properties of a binder are a function of its molecular weight, polymeric morphology and functional groups [31]. Indeed, the high stiffness was attributed to its relatively high molecular weight, and further experiments will be needed to explain the distinct rheological properties possessed by guar gum ceramic pastes.

Both the elastic modulus and yield stress matches the aforementioned desirable rheological properties for a binder. To the author's best knowledge, this is the first study to report the yield stress of an extruded ceramic using DMA. Rheological tools are routinely used to predict the quality of the extrudate, with DMA particularly useful in this context. In addition, the analysis is undemanding in terms of both complexity and sample size. The storage modulus determined was similar to that reported for extrudable hard-metal paste, albeit with a different yield stress [32]. The yield stress is comparable, however, to that found in robocasting and injection moulding [33] [34], but higher than that of tape casting [35]. The rheological properties of GG would be of interest to

researchers working with robocasting, or any other extrusion-based solid free-form fabrication, as a highly viscous, shear-thinning binder is also favoured. Moreover, the wide plasticity of GG infers it may also be used as a plasticiser, providing it does not react with the primary additive.

To summarise the rheological analyses, ceramic pastes with strong shear-thinning properties and a high stiffness can be achieved using guar gum as a binder.

## 4.2 Thermal Debinding and Sintering

### 4.2.1 Thermal Debinding

Having fulfilled its role in shaping and imparting green strength, the binder was then extracted. The process may be achieved through different means but thermal degradation is a fast, reliable method. Thermal stability is proportional to molecular weight, hence high-molecular-weight polymers will require higher temperatures for degradation [31]. Thermal analysis was therefore conducted to determine the degradation characteristics of GG prior to sintering HA.

#### 4.2.1.1 Thermogravimetric Analysis

TGA of the raw guar gum powder was performed in both air and nitrogen gas to elucidate the degradation characteristics (**Fig. 10**). A multi-modal degradation was observed under air (**Fig. 10 (a)**), which is redolent of a heterogeneous polymer structure [36, 37], and culminated into complete degradation by 500 °C. The degradation point is similar to that of methylcellulose [38-40], which is remarkable considering that other high-molecular-weight polymers such as carboxymethyl cellulose degrade at above 1000 °C [41, 42].

11

When analysed under nitrogen gas, approximately 25% of the mass remained until 1000 °C. **Fig. 10 (c)** illustrates discoid pellets comprised of HA and GG heated up to 500 °C in nitrogen which resulted in the formation of a char coating. Thus, it was concluded that complete degradation of GG requires an oxidising atmosphere, and that there was no obvious benefit to applying a two-step debinding treatment comprising both air and nitrogen.

TGA was also performed on HA-GG paste (**Fig. 10 (b)**). An initial loss in mass from ambient temperature to 112 °C was attributed to the evaporation of distilled water. The paste thereafter maintained a constant mass until 228 °C, above which a bimodal loss in mass was observed until 500 °C, and attributed to the degradation of the binder. An imperceptible mass loss was observed from 500 to 1000 °C, which required further analysis to discern the nature thereof, as dehydroxylation of HA was also suspected.

## 4.2.1.2 Fourier-Transformation-Infra-Red Spectroscopy and Scanning Electron Microscopy

FTIR was utilised to verify the degradation behaviour of the paste. The analysis of the raw GG was used to compare to the spectra of crushed extrudates after drying (blue line), and thermally heated to 400 (green line) and 500 °C (red line) (**Fig. 11**). HA troughs were observed at 3570 and 630 cm$^{-1}$ that pertain to the hydroxyl group; and troughs at 1090, 1045, 960, 601 and 570 cm$^{-1}$ were attributed to the phosphate group found therein. The results are indicative of stoichiometric HA [43]. Raw GG troughs that did not overlap with HA peaks were detected at 2925, 1658, 1455 and 815 cm$^{-1}$. The troughs pertaining

to GG are consistent with previous work [44-46]. These troughs were evident in the dried sample, and gradually decreased in the following thermally debound spectra. The data demonstrated that a small quantity of guar gum was present at 500 °C at 2925 and 1658 cm$^{-1}$, whereas the other troughs indicative of GG (red arrows) were absent. However, a noticeable difference in the HA pattern can be observed between 400 and 500 °C, with a clear decrease in OH$^{-}$ trough intensities, which again can explain the subtle mass loss observed between 500 and 1000 °C in **Fig. 10 (c)**. This liberation of the hydroxyl group is known to prefigure the densification of HA.

The presence of GG at 500 °C was further confirmed by SEM imaging of HA pastes after being subject to 500 °C heat. **Fig.** 12 are micrographs depicting the results of discoid pellets fashioned using HA, GG and distilled water that were heated to 400 and 500 °C. At 400 °C, the guar gum was found to firmly adhere and coat the HA particles. Increasing the temperature to 500 °C initiated the degradation of the adhered GG, however, as the image portrays, remnants were still found on the HA particles. Imaging above this temperature was not possible due to samples lacking sufficient green strength for analysis, inferring further progression in degradation. Although not included in this study, FTIR analysis of the sintered HA presented with no evidence of guar gum.

Investigation into the thermal degradation of guar gum revealed that the decomposition of the binder altered in the presence of HA, with the decomposition shifting to higher temperatures. Normally TGA is an adequate method in determining the degradation behaviour of a binder. However, FTIR and SEM were additionally utilised to verify the ambiguous behaviour observed above 500 °C in the thermogram. The outcome of the analyses suggested that an isothermal degradation was required. The

13

extrudates were thermally debound for one hour at 200 and 300, and for three hours at 400 °C. This was to ensure that sufficient time was provided for the binder to degrade, and to avoid using higher temperatures that could result in the densification of HA, as suggested by the FTIR spectra. The following step was to elucidate a suitable heating rate for debinding the extrudates that could lead to a defect-free sintered body.

### 4.2.1.3 Heating Rate

Notwithstanding the debinding temperature, the heating rate is a key determinant in the quality of the final product [31]. Initially, an arbitrary heating rate of 5 °C/min was selected, however, this appeared to facilitate the formation of cracks during debinding, which were later exacerbated during sintering. A slower heating rate of 3 °C/min was trialled, which resulted in an ostensibly defect-free extrudate, however, undetectable cracks became pronounced during sintering in the form of hairline cracks. A further trial at a heating rate of 1 °C/min resulted in a defect-free densified extrudate. This is a common rate in thermal debinding [47-49]. On the other hand, GG is water soluble and thus be of interest where the two-step debinding approach comprising water-debinding is incorporated [50, 51]. The results are outlined in (**Fig. S**).

### 4.3    Scaffold Properties

### 4.3.1   Physical and Mechanical Properties

To further demonstrate the feasibility of GG as a binder during the critical processing steps, we note that its extraction did not adversely affect the periodicity of the porous structure. As **Fig. 13** illustrates, and listed in **Table 1**, the macro-pores maintained their square geometry (640-700 µm), obtained from a die with pin widths of ~ 1000 µm;

thereby shrinking 30-36 %. This far exceeds the desired pore sizes that scaffolds are obligated to possess for rapid bone formation [2, 52], and hence is expected to expedite bone growth. Furthermore, the pore sizes are greater than the width of the walls of the extrudate, and traverse the length of the extrudate. Thus the scaffolds possess a high degree of interconnectivity that provides a continuous path for bone ingrowth [53], as well as the facilitation of the mechanical interlocking between the porous scaffold and the surrounding tissues for enhanced mechanical stability [2, 54]. However, albeit beneficial from a biological perspective, the pore sizes are known to impact the mechanical strength of scaffolds. Thus, depending on the intended clinical application, a balance must be struck between wall thickness and pore size.

To empirically measure the volume fraction of porosity of the extrudates, ~ 4.5 mm cubes were fashioned and the bulk porosity measured using a helium pycnometer. The volume recorded was then subtracted from the apparent volume measured geometrically by a vernier caliper. The mean bulk porosity was determined as 46.5 vol%. The corresponding compressive strength of the cubic scaffolds was 38.6 MPa. In comparison to natural bone, both bulk porosity and compressive strength values are between that of cancellous and cortical bone. Cancellous bone possess higher porosity (50 – 90%) [55], but the compressive strength (2-12 MPa) [56] is notably weaker than cortical bone ( >100 MPa; and a porosity of <30%) [57, 58]. With regards to commercially available bone grafts, the compressive strength was significantly higher. Endobon® is a commercially available hydroxyapatite graft used in replacing bone defects below load-bearing joints (e.g. tibial head fractures). Though the porosity values are similar, Endobon® has a compressive strength that ranges between 1-20 MPa [59].

Thus the extruded HA scaffolds can be used in a similar application with improved mechanical stability.

4.3.2   Microstructure

Fracture surface analysis using SEM (**Fig. 14**) found that an intermediate sintering stage was achieved at 1250 °C. This period precedes complete densification, and is characterised by relatively small sintering necks resulting in micropores [60], as evidenced by the SEM micrographs. Micropores are generally regarded as beneficial for improving in vivo bone growth and overall healing when compared to macropore-only scaffolds [61, 62]; however the case for a microporous topography is inconclusive, with histological analysis determining the relationship between bone healing and micropores as significantly invariable [63]. Both inter- and transgranular fracturing were observed, however, the former was the principle mode of fracturing.

SEM analysis was also employed to examine the morphology of the grains (**Fig. 15**). The microstructure consisted of both a solid and a porous phase. The grain sizes were measured between 1-3 µm, which are comparable to a previous study [64]. However, the same study reported a markedly lower compressive strength.

## 5   Conclusion

GG was successfully applied in the extrusion of a ceramic honeycomb monolith. GG was conducive in the formulation of hydroxyapatite pastes with high stiffness (8.4 MPa) and strong shear-thinning properties desirable in ceramic extrusion and other fabrication techniques. GG also demonstrated satisfactory thermal debinding properties, with a heating rate of 1 °C/min was found to produce crack-free extrudates. The processing steps

opted in this study culminated in densified HA extrudates. In concert with other processing parameters, GG yielded HA scaffolds with compressive strengths (38.6 MPa) and pore sizes (>640 µm) that exceeded that of current commercially available bone grafts. Therefore, a strong justification for the use of guar gum as a binder was presented. With the growing presence of solid free-form techniques, it is envisaged that the potential of GG will expand. Future work will involve investigating the possibility of increasing the ceramic solids loading.

**Acknowledgements**

## 6    References

[1] A.S. Brydone, D. Meek, S. Maclaine, Bone grafting, orthopaedic biomaterials, and the clinical need for bone engineering, Proceedings of the Institution of Mechanical Engineers. Part H, Journal of engineering in medicine, 224 (2010) 1329-1343.

[2] V. Karageorgiou, D. Kaplan, Porosity of 3D biomaterial scaffolds and osteogenesis, Biomaterials, 26 (2005) 5474-5491.

[3] M. Bohner, G. Baroud, A. Bernstein, N. Döbelin, L. Galea, B. Hesse, R. Heuberger, S. Meille, P. Michel, B. von Rechenberg, J. Sague, H. Seeherman, Characterization and distribution of mechanically competent mineralized tissue in micropores of β-tricalcium phosphate bone substitutes, Materials Today.

[4] L.E. Rustom, T. Boudou, S. Lou, I. Pignot-Paintrand, B.W. Nemke, Y. Lu, M.D. Markel, C. Picart, A.J. Wagoner Johnson, Micropore-induced capillarity enhances bone distribution in vivo in biphasic calcium phosphate scaffolds, Acta Biomaterialia, 44 (2016) 144-154.

[5] S.V. Dorozhkin, Bioceramics of calcium orthophosphates, Biomaterials, 31 (2010) 1465-1485.

[6] J. Vivanco, A. Aiyangar, A. Araneda, H.-L. Ploeg, Mechanical characterization of injection-molded macro porous bioceramic bone scaffolds, Journal of the Mechanical Behavior of Biomedical Materials, 9 (2012) 137-152.

[7] M.F. Ashby, Cellular ceramics [electronic resource] : structure, manufacturing, properties and applications, Weinheim : Wiley-VCH, 20052005.

[8] Y. Goto, A. Tsuge, Mechanical Properties of Unidirectionally Oriented SiC-Whisker-Reinforced Si3N4 Fabricated by Extrusion and Hot-Pressing, Journal of the American Ceramic Society, 76 (1993) 1420-1424.

[9] T.M.G. Chu, D.G. Orton, S.J. Hollister, S.E. Feinberg, J.W. Halloran, Mechanical and in vivo performance of hydroxyapatite implants with controlled architectures, Biomaterials, 23 (2002) 1283-1293.

[10] J.M. M. Elbadawi, L. Hopkins and I. Reaney, Progress in Bioactive Metal and, Ceramic Implants for Load- Bearing Application, in: A.R.Z.a.J.B.d. Miranda (Ed.) Advanced Techniques in Bone Regeneration2016.

[11] R. Nath Das, C.D. Madhusoodana, K. Okada, Rheological studies on cordierite honeycomb extrusion, Journal of the European Ceramic Society, 22 (2002) 2893-2900.

[12] A. Aranzabal, D. Iturbe, M. Romero-Sáez, M.P. González-Marcos, J.R. González-Velasco, J.A. González-Marcos, Optimization of process parameters on the extrusion of honeycomb shaped monolith of H-ZSM-5 zeolite, Chemical Engineering Journal, 162 (2010) 415-423.

[13] B.P. Saha, S. Kumari, R. Johnson, N. Eswara Prasad, Effect of relative density on the compressive flow behaviour of cordierite and cordierite: mullite honeycombs, Trans Indian Inst Met, 63 (2010) 701-706.

[14] P. Biswas, K. Rajeswari, V. Mahendar, R. Johnson, Extrusion processing of dense MgAl2O4 spinel honeycombs with low relative density, Ceramics International, 39 (2013) 9819-9821.

[15] W.P. Addiego, W. Liu, T. Boger, Iron oxide-based honeycomb catalysts for the dehydrogenation of ethylbenzene to styrene, Catalysis Today, 69 (2001) 25-31.

[16] S. Ananthakumar, P. Manohar, K.G.K. Warrier, Effect of boehmite and organic binders on extrusion of alumina, Ceramics International, 30 (2004) 837-842.

[17] R. Bayer, M. Knarr, Thermal precipitation or gelling behaviour of dissolved methylcellulose (MC) derivatives—Behaviour in water and influence on the extrusion of ceramic pastes. Part 1: Fundamentals of MC-derivatives, Journal of the European Ceramic Society, 32 (2012) 1007-1018.

[18] M. Knarr, R. Bayer, The shear dependence of the methylcellulose gelation phenomena in aqueous solution and in ceramic paste, Carbohydrate Polymers, 111 (2014) 80-88.

[19] H. Maier, M. Anderson, C. Karl, K. Magnuson, R.L. Whistler, CHAPTER 8 - GUAR, LOCUST BEAN, TARA, AND FENUGREEK GUMS, Industrial Gums (Third Edition), Academic Press, London, 1993, pp. 181-226.

[20] D. Mudgil, S. Barak, B.S. Khatkar, Guar gum: processing, properties and food applications—A Review, Journal of Food Science and Technology, 51 (2014) 409-418.

[21] H. Kono, F. Otaka, M. Ozaki, Preparation and characterization of guar gum hydrogels as carrier materials for controlled protein drug delivery, Carbohydrate Polymers, 111 (2014) 830-840.

[22] J.-H. Zhu, X.-Q. Yang, I. Ahmad, Y. Jiang, X.-Y. Wang, L.-Y. Wu, Effect of guar gum on the rheological, thermal and textural properties of soybean β-conglycinin gel, International Journal of Food Science & Technology, 44 (2009) 1314-1322.

[23] M.J. Ribeiro, J.M. Ferreira, J.A. Labrincha, Plastic behaviour of different ceramic pastes processed by extrusion, Ceramics International, 31 (2005) 515-519.

[24] T.G. Mezger, The Rheology Handbook, Hanover, 2011.

[25] M.M. Rueda, M.-C. Auscher, R. Fulchiron, T. Périé, G. Martin, P. Sonntag, P. Cassagnau, Rheology and applications of highly filled polymers: A review of current understanding, Progress in Polymer Science, 66 (2017) 22-53.

[26] N. Vitorino, C. Freitas, M.J. Ribeiro, J.C.C. Abrantes, J.R. Frade, Extrusion of ceramic emulsions: Plastic behavior, Applied Clay Science, 101 (2014) 315-319.

[27] J. Davies, J.G.P. Binner, Plastic forming of alumina from coagulated suspensions, Journal of the European Ceramic Society, 20 (2000) 1569-1577.

[28] D.J. Horrobin, R.M. Nedderman, Die entry pressure drops in paste extrusion, Chemical Engineering Science, 53 (1998) 3215-3225.

[29] N.K. Mathu, Industrial Galactomannan Polysaccharides, CRC Press2011.

[30] J. Benbow, Paste flow and extrusion, Oxford : Oxford University Press, 1993, Oxford, 1993.

[31] D.J. Shanefield, Organic additives and ceramic processing : with applications in powder metallurgy, ink, and paint, Boston London : Kluwer Academic, c1995, Boston, London, 1995.

[32] H. Biermann, U. Martin, C.G. Aneziris, A. Kolbe, A. Müller, W. Schärfl, M. Herrmann, Microstructure and Compression Strength of Novel TRIP-Steel/Mg-PSZ Composites, Advanced Engineering Materials, 11 (2009) 1000-1006.

[33] A. Diaz-Cano, R.W. Trice, J.P. Youngblood, Stabilization of highly-loaded boron carbide aqueous suspensions, Ceramics International.

[34] E. Feilden, E.G.-T. Blanca, F. Giuliani, E. Saiz, L. Vandeperre, Robocasting of structural ceramic parts with hydrogel inks, Journal of the European Ceramic Society, 36 (2016) 2525-2533.

[35] A. Zupancic, R. Lapasin, A. Kristoffersson, Influence of particle concentration on rheological properties of aqueous α-Al2O3 suspensions, Journal of the European Ceramic Society, 18 (1998) 467-477.

[36] G.R. Filho, R.M.N. de Assunção, J.G. Vieira, C.d.S. Meireles, D.A. Cerqueira, H. da Silva Barud, S.J.L. Ribeiro, Y. Messaddeq, Characterization of methylcellulose produced from sugar cane bagasse cellulose: Crystallinity and thermal properties, Polymer Degradation and Stability, 92 (2007) 205-210.

[37] M. Trunec, J. Cihlar, Thermal removal of multicomponent binder from ceramic injection mouldings, Journal of the European Ceramic Society, 22 (2002) 2231-2241.

[38] S.-Y. Lin, S.-L. Wang, Y.-S. Wei, M.-J. Li, Temperature effect on water desorption from methylcellulose films studied by thermal FT-IR microspectroscopy, Surface Science, 601 (2007) 781-785.

[39] G. Rioland, T.J. Daou, D. Faye, J. Patarin, A new generation of MFI-type zeolite pellets with very high mechanical performance for space decontamination, Microporous and Mesoporous Materials, 221 (2016) 167-174.

[40] J.-H. Feng, L.G. Ferguson, F. Dogan, Processing of buffer sheets for sintering of PLZT tapes, Journal of Materials Processing Technology, 110 (2001) 47-52.

[41] N. Ninan, M. Muthiah, I.-K. Park, A. Elain, S. Thomas, Y. Grohens, Pectin/carboxymethyl cellulose/microfibrillated cellulose composite scaffolds for tissue engineering, Carbohydrate Polymers, 98 (2013) 877-885.

[42] W.P.F. Neto, H.A. Silvério, J.G. Vieira, H. da Costa e Silva Alves, D. Pasquini, R.M.N. de Assunção, N.O. Dantas, Preparation and Characterization of Nanocomposites of Carboxymethyl Cellulose Reinforced with Cellulose Nanocrystals, Macromolecular Symposia, 319 (2012) 93-98.

[43] S. Pramanik, A.K. Agarwal, K.N. Rai, A. Garg, Development of high strength hydroxyapatite by solid-state-sintering process, Ceramics International, 33 (2007) 419-426.

[44] V. Singh, A. Singh, S. Joshi, T. Malviya, Grafting of vinyl acetate-ethylacrylate binary monomer mixture onto guar gum, International Journal of Biological Macromolecules, 84 (2016) 442-447.

[45] A.G. Sullad, L.S. Manjeshwar, T.M. Aminabhavi, Microspheres of carboxymethyl guar gum for in vitro release of abacavir sulfate: Preparation and characterization, Journal of Applied Polymer Science, 122 (2011) 452-460.

[46] B.S. Kaith, R. Sharma, S. Kalia, Guar gum based biodegradable, antibacterial and electrically conductive hydrogels, International Journal of Biological Macromolecules, 75 (2015) 266-275.

[47] P. Biswas, K. Rajeswari, P. Ramavath, R. Johnson, H.S. Maiti, Fabrication of Transparent Spinel Honeycomb Structures by Methyl Cellulose–Based Thermal Gelation Processing, Journal of the American Ceramic Society, 96 (2013) 3042-3045.

[48] Y. Du, N.M. Sammes, Fabrication of tubular electrolytes for solid oxide fuel cells using strontium- and magnesium-doped LaGaO3 materials, Journal of the European Ceramic Society, 21 (2001) 727-735.

[49] M. Ray, P. Bhattacharya, R. Das, K. Sondhi, S. Ghosh, S. Sarkar, Preparation and characterization of macroporous pure alumina capillary membrane using boehmite as binder for filtration application, Journal of Porous Materials, 22 (2015) 1043-1052.

[50] W. Liu, X. Yang, Z. Xie, C. Jia, L. Wang, Novel fabrication of injection-moulded ceramic parts with large section via partially water-debinding method, Journal of the European Ceramic Society, 32 (2012) 2187-2191.

[51] M.M. Shbeh, R. Goodall, Design of water debinding and dissolution stages of metal injection moulded porous Ti foam production, Materials & Design, 87 (2015) 295-302.

[52] P.S. EGGLI, W. MOLLER, R.K. SCHENK, Porous Hydroxyapatite and Tricalcium Phosphate Cylinders with Two Different Pore Size Ranges Implanted in the Cancellous Bone of Rabbits: A Comparative Histomorphometric and Histologic Study of Bony Ingrowth and Implant Substitution, Clinical Orthopaedics and Related Research, 232 (1988) 127-138.

[53] G. Hannink, J.J.C. Arts, Bioresorbability, porosity and mechanical strength of bone substitutes: What is optimal for bone regeneration?, Injury, 42, Supplement 2 (2011) S22-S25.

[54] Q.L. Loh, C. Choong, Three-Dimensional Scaffolds for Tissue Engineering Applications: Role of Porosity and Pore Size, Tissue Engineering. Part B, Reviews, 19 (2013) 485-502.

[55] X. Wang, S. Xu, S. Zhou, W. Xu, M. Leary, P. Choong, M. Qian, M. Brandt, Y.M. Xie, Topological design and additive manufacturing of porous metals for bone scaffolds and orthopaedic implants: A review, Biomaterials, 83 (2016) 127-141.

[56] L. Røhl, E. Larsen, F. Linde, A. Odgaard, J. Jørgensen, Tensile and compressive properties of cancellous bone, Journal of Biomechanics, 24 (1991) 1143-1149.

[57] R. Havaldar, S.C. Pilli, B.B. Putti, Insights into the effects of tensile and compressive loadings on human femur bone, Advanced Biomedical Research, 3 (2014) 101.

[58] X. Wang, Q. Ni, Determination of cortical bone porosity and pore size distribution using a low field pulsed NMR approach, Journal of Orthopaedic Research, 21 (2003) 312-319.

[59] T. Kurien, R.G. Pearson, B.E. Scammell, Bone graft substitutes currently available in orthopaedic practice The evidence for their use, The bone and Joint Journal, 95-B (2013) 583-597.

[60] M.N. Rahaman, Ceramic Processing and Sintering, Taylor & Francis Group, Florida, 2003.

[61] S.K. Lan Levengood, S.J. Polak, M.J. Poellmann, D.J. Hoelzle, A.J. Maki, S.G. Clark, M.B. Wheeler, A.J. Wagoner Johnson, The effect of BMP-2 on micro- and macroscale osteointegration of biphasic calcium phosphate scaffolds with multiscale porosity, Acta Biomaterialia, 6 (2010) 3283-3291.

[62] B. Annaz, K.A. Hing, M. Kayser, T. Buckland, L.D. Silvio, Porosity variation in hydroxyapatite and osteoblast morphology: a scanning electron microscopy study, Journal of Microscopy, 215 (2004) 100-110.

[63] J.G. Dellinger, J.A.C. Eurell, R.D. Jamison, Bone response to 3D periodic hydroxyapatite scaffolds with and without tailored microporosity to deliver bone morphogenetic protein 2, Journal of Biomedical Materials Research Part A, 76A (2006) 366-376.

[64] Q. Wu, X. Zhang, B. Wu, W. Huang, Effects of microwave sintering on the properties of porous hydroxyapatite scaffolds, Ceramics International, 39 (2013) 2389-2395.

**Figure Captions**

**Table Caption**

**Fig. 1.** SEM (SE) micrographs depicting the powder morphology of guar gum, at low **(a)** and high **(b)** magnification.



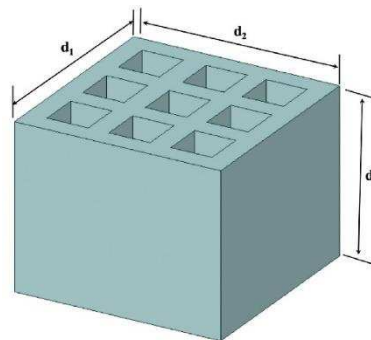**Fig. 2.** CAD model of the honeycomb die used.



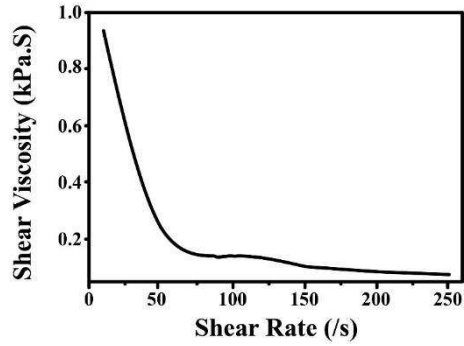**Fig. 3.** Schematic illustrating the dimensions used to determine the apparent volume.

**Fig. 4.** Viscosity rheogram of hydroxyapitite-guar gum pastes. The figure illustrate the change in shear viscosity ($\eta$) as a function of shear rate ($\gamma$).
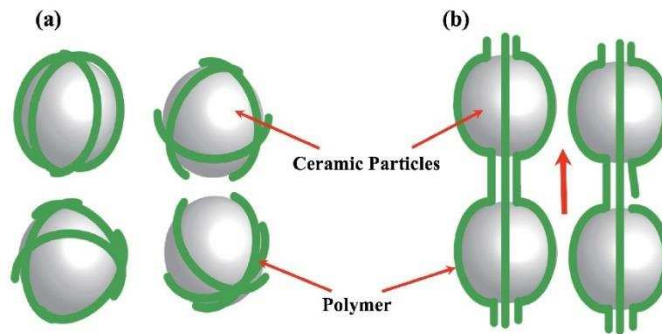


**Fig. 5.** Illustration of the effects of extrusion on binder orientation. Shear-thinning occurs when the polymers are entangled and oriented in different directions. Once the polymers are disentangled, and oriented in the direction of extrusion, the paste can flow. Flow has to be achieved without tear to the chain to prevent lamination, hence, a wide plasticity region is favoured.
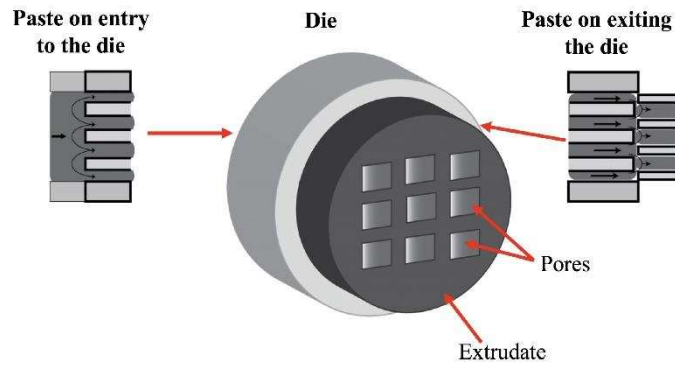
**Fig. 6.** Schematic demarcating the behaviour of the paste during honeycomb extrusion.
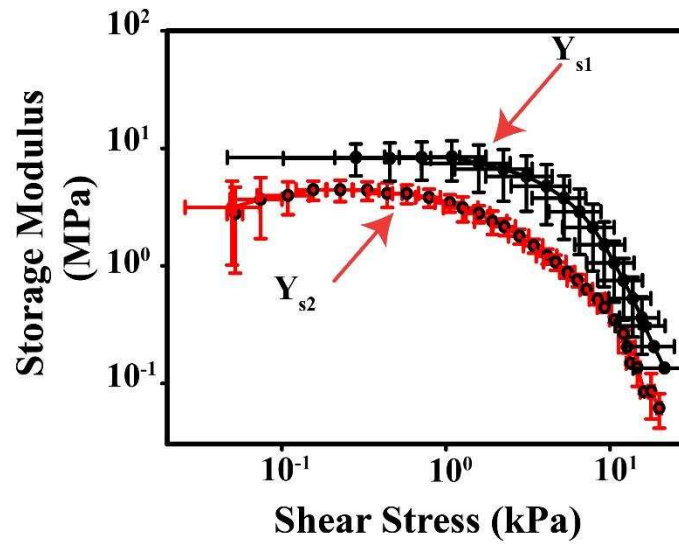


**Fig. 7.** Dynamic Mechanical Analysis of HA-GG pastes. The storage modulus was recorded as a function of shear stress. $Y_{s1}$ pertains to the yield stress of the initial paste, and $Y_{s2}$ is the yield stress of pastes having previously subjected to shearing.
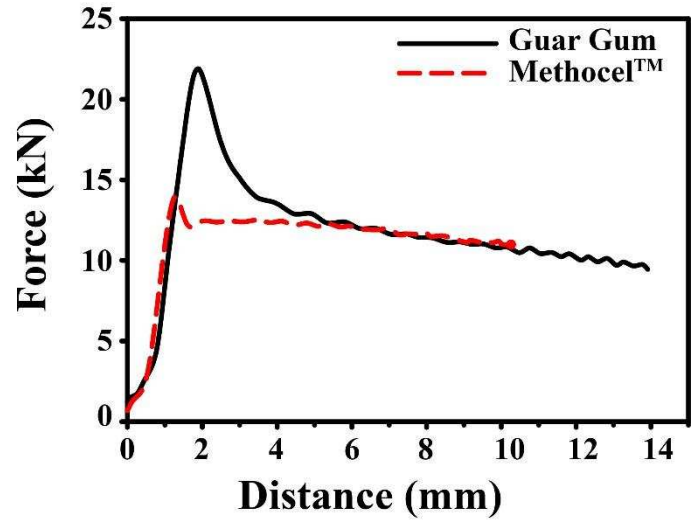
**Fig. 8.** Representative extrusion plots recorded during paste extrusion.
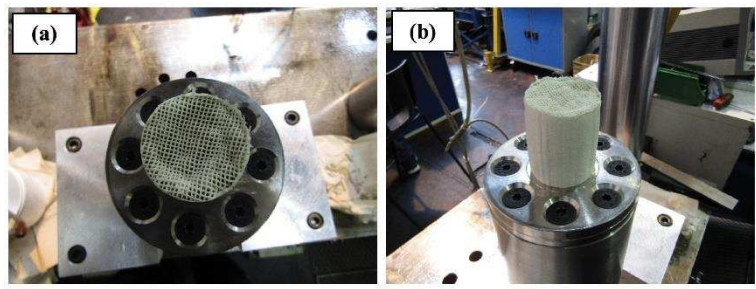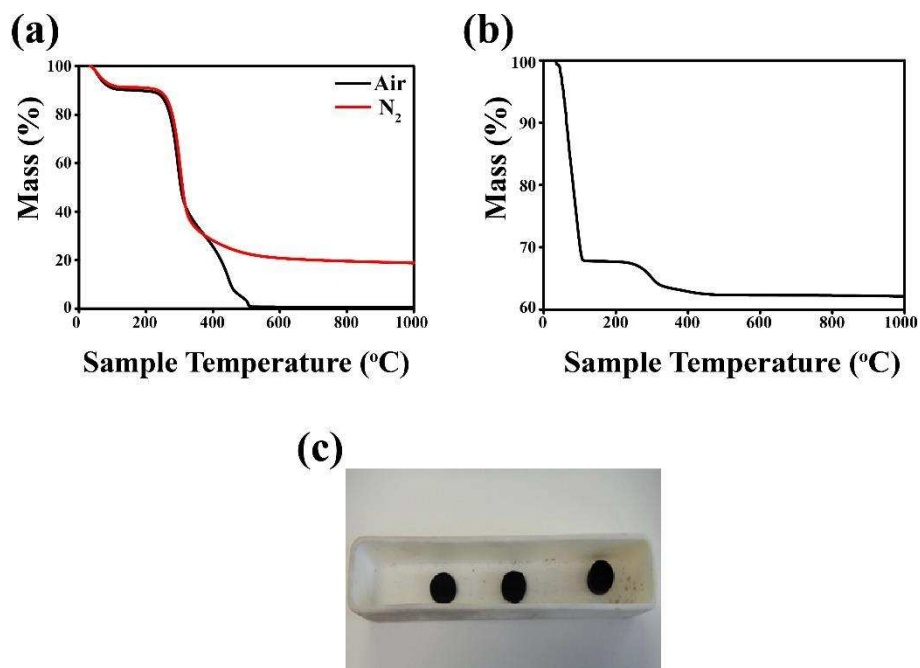


**Fig. 9.** Honeycomb extrudates using guar gum as the binder.

**Fig. 10.** TGA analysis of the raw binder **(a)** and paste **(b)**, and the results of pellets thermally debound in nitrogen atmosphere **(c)**.
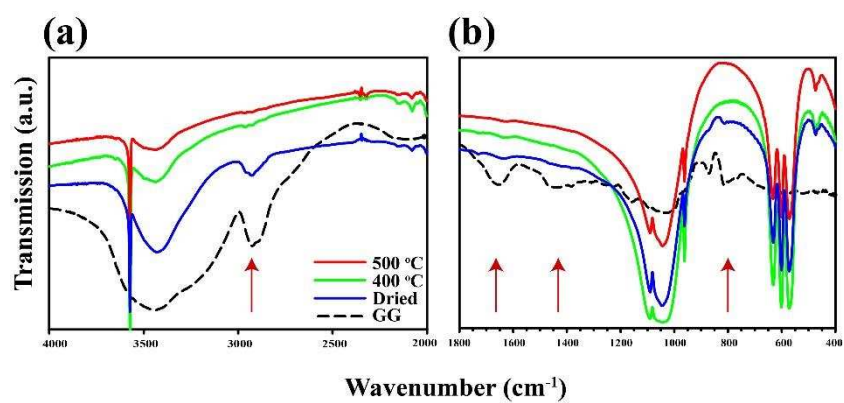


**Fig. 11.** FTIR spectra of the raw guar gum (dashed), and pastes after drying (blue), thermal debinding at 400 (green), and at 500 °C (red).
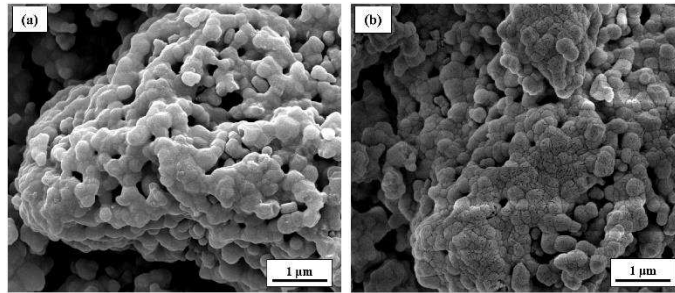
29

**Fig.** 12. SEM (SE) micrographs of the paste after thermally debinding at 400 **(a)** and 500 °C **(b)**.
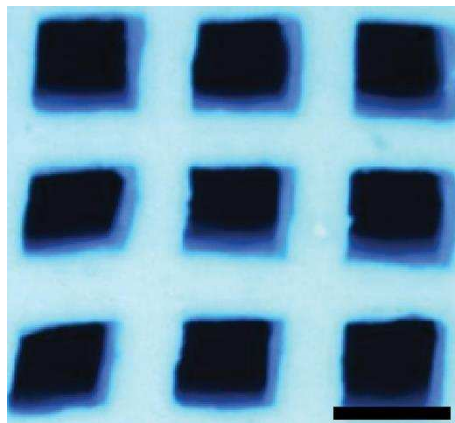


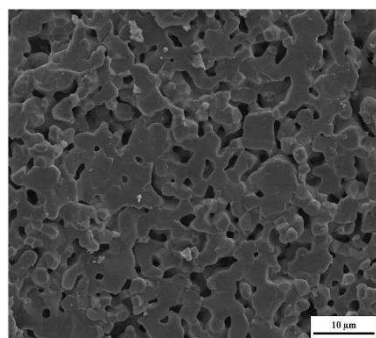**Fig. 13.** Optical microscope portraying the macro-pore sizes (scale bare = 1 mm).



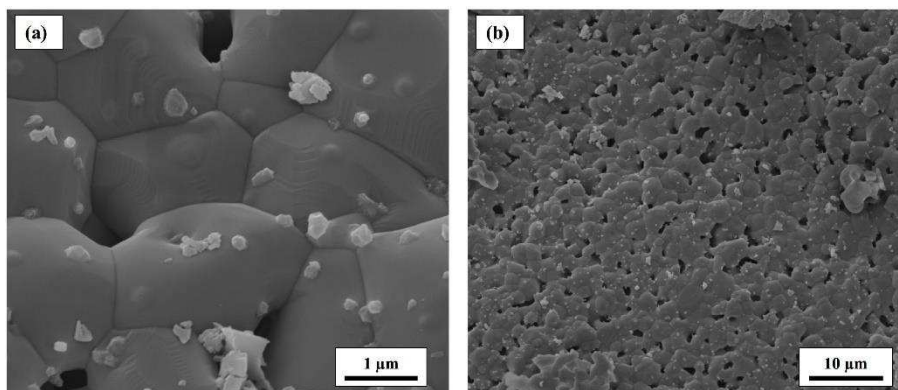**Fig. 14.** SEM (SE) micrograph depicting the fracture surface.

**Fig. 15.** SEM (SE) micrographs highlighting the grain morphology of the sintered HA body, at high **(a)** and low **(b)** magnification.

**Table 1.**

Scaffold physical and mechanical properties.

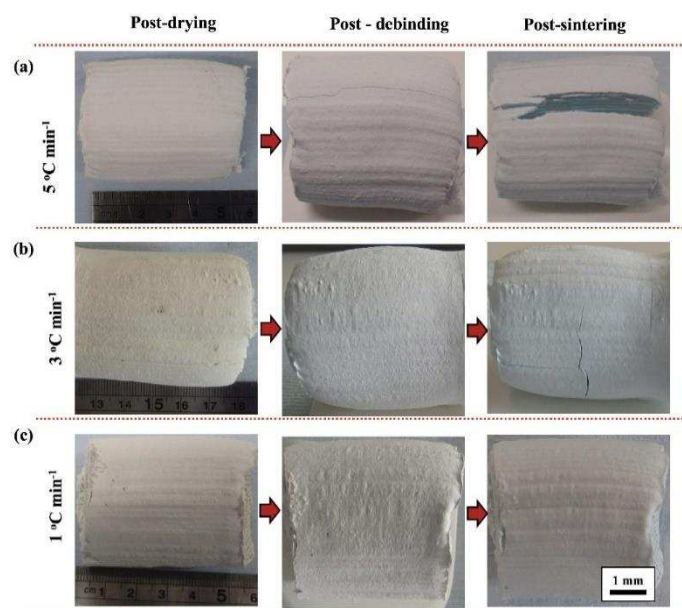| Cell Length (µm) | Strut Thickness (µm) | Bulk Porosity (%) | Compressive Strength (MPa) |
|---|---|---|---|
| 717 ± 72 | 528 ± 32 | 46.5 ± 1.2 | 38.6 ± 6.1 |

**Fig. S1.** Images illustrating the effects of heating rate during debinding on the extrudates.